

Highly Responsive Polar Vortices in All-Ferroelectric Heterostructures

Pravin Kavle, Aiden M. Ross, Harikrishnan KP, Peter Meisenheimer, Arvind Dasgupta, Jiyuan Yang, Ching-Che Lin, Hao Pan, Piush Behera, Eric Parsonnet, Xiaoxi Huang, Jacob A. Zorn, Yu-Tsun Shao, Sujit Das, Shi Liu, David A. Muller, Ramamoorthy Ramesh, Long-Qing Chen, and Lane W. Martin*

The discovery of polar vortices and skyrmions in ferroelectric-dielectric superlattices [such as $(\text{PbTiO}_3)_n/(\text{SrTiO}_3)_n$] has ushered in an era of novel dipolar topologies and corresponding emergent phenomena. The key to creating such emergent features has generally been considered to be related to counterpoising strongly polar and non-polar materials thus creating the appropriate boundary conditions. This limits the utility these materials can have, however, by rendering (effectively) half of the structure unresponsive to applied stimuli. Here, using advanced thin-film deposition and an array of characterization and simulation approaches, polar vortices are realized in all-ferroelectric trilayers, multilayers, and superlattices built from the fundamental building block of $(\text{PbTiO}_3)_n/(\text{Pb}_x\text{Sr}_{1-x}\text{TiO}_3)_n$ wherein in-plane ferroelectric polarization in the $\text{Pb}_x\text{Sr}_{1-x}\text{TiO}_3$ provides the appropriate boundary conditions. These superlattices exhibit substantially enhanced electromechanical and ferroelectric responses in the out-of-plane direction that arise from the ability of the polarization in both layers to rotate to the out-of-plane direction under field. In the in-plane direction, the layers are found to be strongly coupled during switching and when heterostructured with ferroelectric-dielectric building blocks, it is possible to produce multistate switching. This approach expands the realm of systems supporting emergent dipolar texture formation and does so with entirely ferroelectric materials thus greatly improving their responses.

1. Introduction

Emergent topological polar textures, including vortices,^[1] dipolar waves,^[2] skyrmions,^[3] merons,^[4] and others, have generated considerable interest.^[5] Thus far, ferroelectric-dielectric superlattices including those based on $(\text{PbTiO}_3)_n/(\text{SrTiO}_3)_n$ have served as the model system for this work^[1] wherein the delicate balance of electric, elastic, and gradient energies can be tailored to manipulate the order parameter.^[1–4] The resulting emergent polar textures also exhibit novel phenomena including coexistence of phases,^[6] chirality,^[7] negative capacitance,^[8,9] and emergent driven phases,^[10] modes^[11] and anisotropic ferroelectric polarization switching along and perpendicular to polar vortices.^[12] The intimate interactions and competition between the strongly polar ferroelectric and non-polar dielectric are thought to be essential for the formation of these features. The fact that half of such superlattices are

P. Kavle, P. Meisenheimer, A. Dasgupta, C.-C. Lin, H. Pan, P. Behera, X. Huang, R. Ramesh, L. W. Martin
 Department of Materials Science and Engineering
 University of California
 Berkeley, CA 94720, USA
 E-mail: lwmartin@rice.edu

A. M. Ross, J. A. Zorn, L.-Q. Chen
 Department of Materials Science and Engineering
 The Pennsylvania State University
 University Park, PA 16802, USA

H. KP, D. A. Muller
 Department of Applied and Engineering Physics
 Cornell University
 Ithaca, NY 14853, USA

J. Yang, S. Liu
 Key Laboratory for Quantum Materials of Zhejiang Province
 Department of Physics
 School of Science and Research Center for Industries of the Future
 Westlake University
 Hangzhou, Zhejiang 310030, China

E. Parsonnet, R. Ramesh
 Department of Physics
 University of California
 Berkeley, CA 94720, USA
 Y.-T. Shao
 Mork Family Department of Chemical Engineering and Materials Science
 University of Southern California
 Los Angeles, CA 90089, USA

S. Das
 Materials Research Centre
 Indian Institute of Science
 Bangalore 560012, India

 The ORCID identification number(s) for the author(s) of this article can be found under <https://doi.org/10.1002/adma.202410146>

DOI: 10.1002/adma.202410146

essentially unresponsive to, for example, electric fields (except in a simple linear-dielectric fashion) means that these structures cannot be readily manipulated and have limited to small effects only in certain directions.^[13] At the same time, however, similar polar textures have also been found in ferroelectric-metal superlattices based on $(\text{PbTiO}_3)_n/(\text{SrRuO}_3)_n$,^[14,15] but again these materials have limited response to applied fields due to the presence of the periodic metallic layers. This begs the question as to how these novel polar textures can be better controlled using applied fields?

One pathway may be to explore ferroelectric-ferroelectric heterostructures wherein both layers are robustly polar and responsive to applied fields. In fact, researchers have already explored multilayer ferroelectric heterostructures with the goal of manipulating their properties and exploiting the potential for coupling across interfaces. For example, in bilayers based on the $\text{PbZr}_y\text{Ti}_{1-y}\text{O}_3$ system, heterostructures consisting of tetragonal ($y = 0.3$) and rhombohedral ($y = 0.7$) layers showed enhanced piezoelectric response due to increased ferroelastic-domain activity^[16] and deterministic reorientation of ferroelastic domain walls.^[17] Other $\text{PbZr}_y\text{Ti}_{1-y}\text{O}_3$ bilayer heterostructures (with $y = 0.2$ and $y = 0.8$ layers) exhibited tunable structural, dielectric, and ferroelectric properties upon altering the order of the films.^[18] In $\text{Pb}_x\text{Sr}_{1-x}\text{TiO}_3$ bilayers, interlayer coupling-induced exchange-bias-like phenomena.^[19] It remains to be seen, however, if emergent polar structures can be produced in these all-ferroelectric superlattices and, if they can, how this impacts their overall response to applied stimuli?

Here, polar vortices are realized in all-ferroelectric trilayers, multilayers, and superlattices constructed from $(\text{PbTiO}_3)_n/(\text{Pb}_x\text{Sr}_{1-x}\text{TiO}_3)_n$ ($x = 0.2, 0.3, 0.4, 0.5, \text{ and } 0.6$; $n = 16$) building blocks, where the $\text{Pb}_x\text{Sr}_{1-x}\text{TiO}_3$ layers exhibit robust, in-plane polarization, but still provide the boundary conditions to support vortex formation in the PbTiO_3 . Scanning transmission electron microscopy (STEM)-based imaging and ptychography are used to directly image the emergent-vortex structures. In turn, both the out-of- and in-plane responses to applied fields are probed. In the out-of-plane direction, all-ferroelectric superlattices exhibit electromechanical and

polarization responses that increase systematically with x ultimately being as much as 7.5- and 2.4-times higher, respectively, than similar ferroelectric-dielectric superlattices. Phase-field and molecular-dynamics (MD) simulations reveal that these effects arise from the ability of the polarization in both layers to rotate freely from their ground states (vortex or in-plane polarized) to the out-of-plane direction. In the in-plane direction, exotic coupling and switching behavior is observed. The net-in-plane-polarization components of the vortices in the PbTiO_3 ^[13] (which is related to the vertical shifting of the vortices in the layer) and the in-plane domains in the $\text{Pb}_x\text{Sr}_{1-x}\text{TiO}_3$ layers^[19] exhibit strong elastic and dipolar coupling. Phase-field and MD simulations again reveal the nature of this coupling and how it responds under field with impacts being found on the overall vortex periodicity, coercivity, and subsequent collective-switching pathways. In multilayers with controlled thicknesses of SrTiO_3 inserted between ferroelectric-ferroelectric and ferroelectric-dielectric building blocks, it is possible to control the strength of that coupling and to realize exotic effects including multi-state polarization switching and stability taking advantage of the different polarization reversal mechanisms in each type of structure.

2. Results and Discussion

For this work, the fundamental building block is $(\text{PbTiO}_3)_n/(\text{Pb}_x\text{Sr}_{1-x}\text{TiO}_3)_n$ ($x = 0, 0.2, 0.3, 0.4, 0.5, \text{ and } 0.6$; $n = 16$) all grown on DyScO_3 (110) substrates (Experimental Section). Here, a naming convention wherein the chemistry (x) and (as needed) the number of repeats (p) are denoted together with a qualifying description. For example, trilayers of the form $(\text{Pb}_{0.3}\text{Sr}_{0.7}\text{TiO}_3)_{16}/(\text{PbTiO}_3)_{16}/(\text{Pb}_{0.3}\text{Sr}_{0.7}\text{TiO}_3)_{16}$ are referred to as $x = 0.3$ trilayers (Figure 1a), multilayers of the form $(\text{Pb}_{0.3}\text{Sr}_{0.7}\text{TiO}_3)_{16}/(\text{PbTiO}_3)_{16}/(\text{Pb}_{0.3}\text{Sr}_{0.7}\text{TiO}_3)_{16}/(\text{SrTiO}_3)_{16}/(\text{PbTiO}_3)_{16}/(\text{SrTiO}_3)_{16}$ are referred to as $x = 0.3/0$ multilayers, and superlattices of the form $[(\text{PbTiO}_3)_{16}/(\text{Pb}_{0.3}\text{Sr}_{0.7}\text{TiO}_3)_{16}]_5$ are referred to as $x = 0.3, p = 5$ superlattices. To compare the evolution of the structures with varying chemistry, X-ray diffraction reciprocal space maps (RSMs, Experimental Section) about the 002_{pc} -diffraction condition of the DyScO_3 substrate and along the in-plane direction ($H, [100]_{\text{pc}}$) were completed for a number of trilayers (where pc refers to pseudocubic indices). As a reference, studies of $x = 0$ trilayers reveal satellite peaks corresponding to vortices of period 11.4 nm (Figure 1b). Upon transitioning to $x = 0.3$ (Figure 1c) and $x = 0.5$ trilayers, studies also reveal satellite peaks corresponding to vortices but with periodicities of 13.4 and 37.5 nm, respectively (RSMs for $x = 0, 0.2, 0.3, 0.4, 0.5, \text{ and } 0.6$ trilayers are provided; Figure S1, Supporting Information). Upon further increasing the lead content as in $x = 0.6$ trilayers, however, the structure transforms into periodic c/a domains (Figure 1d). The evolution of vortex periodicity with chemistry is summarized (Figure 1e). Additional RSM studies and associated structural details for trilayers (Figures S2 and S3, Supporting Information) and superlattices of varying chemistries revealing similar structural periodicity trends (Figures S4 and S5, Supporting Information) are also provided. All told, such studies point toward the formation of vortices in all-ferroelectric heterostructures.

S. Liu
Institute of Natural Sciences
Westlake Institute for Advanced Study
Hangzhou, Zhejiang 310024, China

D. A. Muller
Kavli Institute at Cornell for Nanoscale Science
Ithaca, NY 14853, USA

R. Ramesh, L. W. Martin
Departments of Materials Science and NanoEngineering and Physics and Astronomy
Rice University
Houston, TX 77005, USA

R. Ramesh, L. W. Martin
Rice Advanced Materials Institute
Rice University
Houston, TX 77005, USA

L. W. Martin
Department of Chemistry
Rice University
Houston, TX 77005, USA

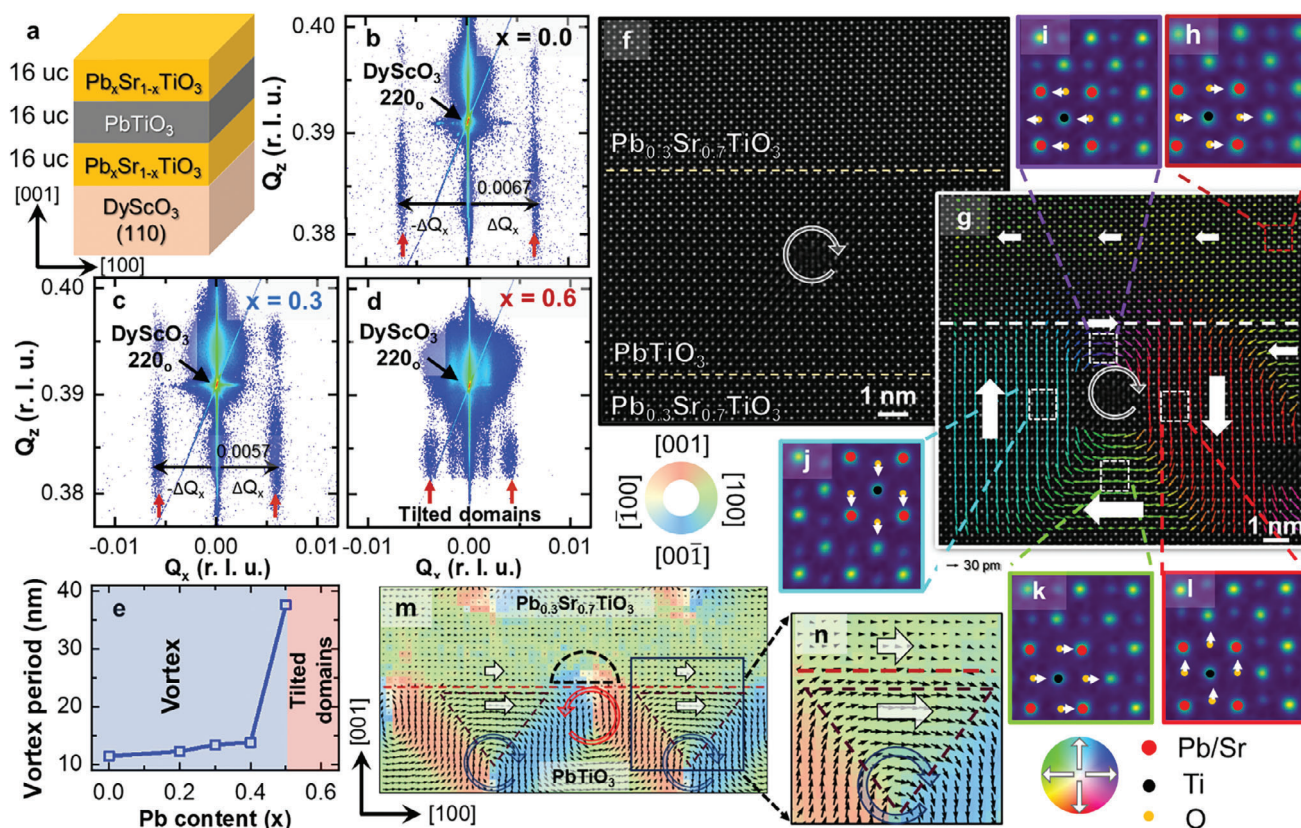


Figure 1. a) Schematic illustration of the $x = 0.3$ trilayers. 2D reciprocal space maps (RSMs) about the 220_{O} -diffraction condition of DyScO_3 (110) with a pair of vertical red arrows representing vortex periodicity for b) $x = 0$, c) $x = 0.3$, and d) $x = 0.6$ trilayers, with the latter showing tilted c/a -domains. e) Vortex periodicity measured as a function of the lead content (x) for the trilayer system. f) Ptychographic reconstructed image of the $x = 0.3$ trilayers with the white rotating arrow showing the lattice distortion corresponding to the vortex core. g) Ptychographic reconstructed image shows the displacement of the centroid of the A-site cations with respect to the centroid of the oxygen atoms mapped out for each pseudo-cubic unit cell. Zoom-in regions showing pseudo-cubic unit cells with different atoms having specific color codes for the h) $\text{Pb}_{0.3}\text{Sr}_{0.7}\text{TiO}_3$ region, i) vortex top side, j) vortex left side, k) vortex bottom side, and l) vortex right side. Molecular-dynamics (MD) simulations revealing m) vortex formation in the PbTiO_3 layer and in-plane domains in the $\text{Pb}_{0.3}\text{Sr}_{0.7}\text{TiO}_3$ layer for $x = 0.3$ trilayers along with n) a zoom-in of the region at the interface region showing alignment of in-plane components in the same direction.

To confirm that the observed satellite peaks arise from vortex formation, the polarization was analyzed at the atomic scale (Figures S6 and S7, Supporting Information) using scanning transmission electron microscopy-based multislice electron ptychography^[20,21] for a representative $x = 0.3$ trilayer (Figure 1f) (Experimental Section). The atomic displacement map (Figure 1g) is created based on the distances between the centroid of the oxygen anions to the centroid of the A-site (lead, strontium) cations for each pseudo-cubic unit cell and it reveals the presence of vortex-like texture in the PbTiO_3 and in-plane polarization in the $\text{Pb}_{0.3}\text{Sr}_{0.7}\text{TiO}_3$. Other displacement maps (Figure S8, Supporting Information) and maps obtained with annular dark field (ADF) imaging are also provided (Figures S9 and S10, Supporting Information). The enlarged 2×2 pseudocubic unit cell in the $\text{Pb}_{0.3}\text{Sr}_{0.7}\text{TiO}_3$ layer (Figure 1h) shows displacement of oxygen atoms in relation to the cations (highlighted by the small white arrows), showing the presence of in-plane polarization. In the PbTiO_3 layer (Figure 1i–l), a large magnitude of the displacement (≈ 40 pm) is observed which changes in direction as one transits about the vortex core. In turn, a net in-plane polarization

in the PbTiO_3 layer (here, pointing from right to left) is aligned with the polarization in the $\text{Pb}_{0.3}\text{Sr}_{0.7}\text{TiO}_3$ layer. All told, the STEM-based imaging confirms the formation of a novel emergent polarization texture in all-ferroelectric heterostructures.

To better understand how the vortices form and their evolution with chemistry and periodicity, MD simulations were carried out for $x = 0$ – 0.7 superlattices (Figure S11, Supporting Information and Experimental Section). For example, in $x = 0.3$ superlattices (Figure 1m), the equilibrium state includes vortices in the PbTiO_3 and in-plane polarized ferroelectric domains in the $\text{Pb}_{0.3}\text{Sr}_{0.7}\text{TiO}_3$; consistent with the X-ray and STEM findings. Similar vortices are observed for $x = 0$ – 0.5 superlattices (Figure S11a–f, Supporting Information) before the structure transitions into periodic c/a domains throughout both layers for $x = 0.6$ – 0.7 superlattices (Figure S11g,h, Supporting Information). The staggered vortex configuration (Figure 1m) along with alternating clockwise (rotating blue arrows) and counterclockwise (rotating red arrows) leads to a net in-plane polarization^[13] along the $[100]_{\text{pc}}$. As the $\text{Pb}_x\text{Sr}_{1-x}\text{TiO}_3$ adopts a more pronounced in-plane orientation with increasing lead content (x), the

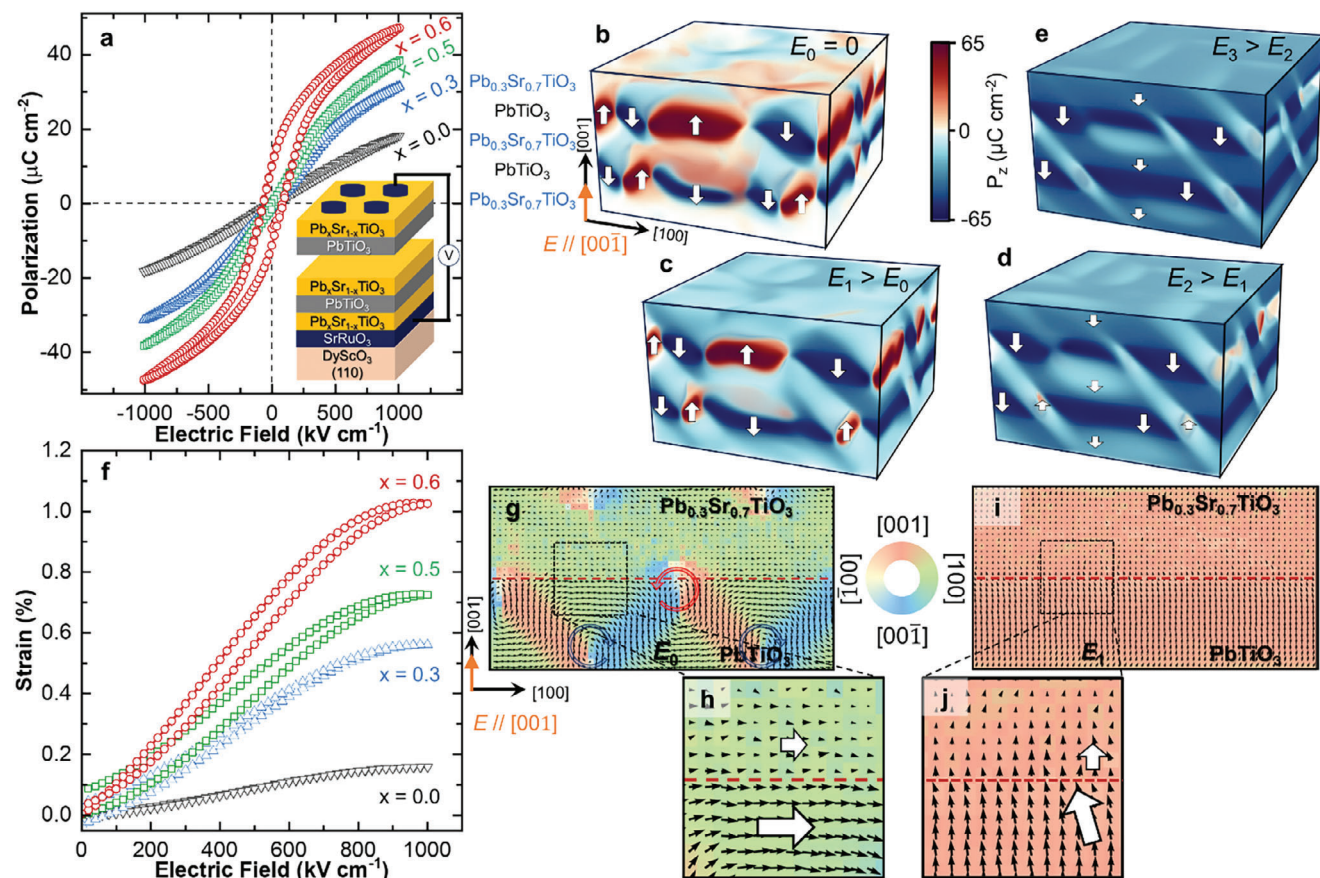


Figure 2. a) Out-of-plane polarization-electric field hysteresis loops measured at 10 kHz for $x = 0, 0.3, 0.5,$ and $0.6, p = 5$ superlattices. Various switching steps are as extracted from phase-field simulations at different electric field starting with b) the initial state at E_0 , c) intermediate stage at $E_1 > E_0$, d) next intermediate stage at $E_2 > E_1$, and e) final state at $E_3 > E_2$. f) Electromechanical strain (in percent) -electric field loops measured for $x = 0, 0.3, 0.5,$ and $0.6, p = 5$ superlattices. Corresponding MD simulations displaying out-of-plane switching of the $x = 0.3$ superlattices starting with g) the initial state at E_0 with h) a zoom-in area around the interface and i) the final state at E_1 with j) a zoom-in area around the interface at fully switched state.

in-plane substructure of the PbTiO_3 layer (dashed brown triangles, Figure 1m,n) enlarges to maintain polarization continuity across the interface. The strain boundary condition being applied to the PbTiO_3 by the DyScO_3 substrates favors c/a domain formation (i.e., a mixture of in- and out-of-plane polarized regions) which ultimately manifests as vortices in these confined heterostructures. The presence of the out-of-plane polarized regions further compels regions within $\text{Pb}_{0.3}\text{Sr}_{0.7}\text{TiO}_3$ near the interface to undergo local polarization rotation (black, dotted half circle, Figure 1m), leading to additional gradient energy. Therefore, this rearrangement of polarization is induced via short-range interactions at the interfaces and favors larger period vortex structures with increasing lead content (x) before transitioning the structure into periodic c/a domains (Figure S12, Supporting Information).

Having established that novel, emergent vortex order can be produced in all-ferroelectric heterostructures, the question of whether these heterostructures are correspondingly more responsive to applied fields remains. To explore this question, out-of-plane capacitor structures (Experimental Section) were produced to probe the out-of-plane polarization-electric field evolution (Figure 2a and Experimental Section). Classic $x = 0, p = 5$ superlattices exhibit linear-dielectric-like response and serve

as the reference state (black data, Figure 2a), while $x = 0.3$ and $0.5, p = 5$ superlattices exhibit increased saturation polarization (P_s) and response that is antiferroelectric-like in nature (as substantiated by switching-current loops which show four peaks in one complete loop, two on each side; Figure S13a, Supporting Information). This antiferroelectric-like response is assigned to the out-of-plane switching of the originally in-plane polarized $\text{Pb}_x\text{Sr}_{1-x}\text{TiO}_3$ layers along with the switching of the vortices. Further increasing the lead content, as in $x = 0.6, p = 5$ superlattices, reveals ferroelectric-like switching (again substantiated by switching-current loops which show two peaks in one complete loop, one on each side; Figure S13a, Supporting Information) which matches well with the anticipated c/a -domain structure. These artificial electrostatically engineered antiferroelectric-like heterostructures^[22] with ferroelectric polar vortices also show enhanced energy storage which is maximized for $x = 0.5$ heterostructures before decreasing for $x = 0.6$ heterostructures commensurate with the transition from vortices to c/a domain architectures (Figure S13b, Supporting Information).

The polarization-electric field evolution can be further analyzed using phase-field simulations (Experimental Section).

Here, the simulations explore a $x = 0.3$ superlattice wherein the applied field increases 50 kV cm^{-1} every 100-time steps until it reaches 1000 kV cm^{-1} , then decreases at the same rate to -1000 kV cm^{-1} , before returning to 0 kV cm^{-1} to form a complete switching cycle. Starting with electric field $E_0 = 0 \text{ kV cm}^{-1}$ (Figure 2b), vortices are observed in the PbTiO_3 layers by analyzing the P_z component. With $E_1 = 300 \text{ kV cm}^{-1}$ applied along the $[001]_{\text{pc}}$ (after 600-time steps), the fraction of the downward polarized area in the PbTiO_3 layers increases at the same time as there is initiation of downward polarization in the $\text{Pb}_{0.3}\text{Sr}_{0.7}\text{TiO}_3$ layers (Figure 2c). Upon further increasing the field to $E_2 = 650 \text{ kV cm}^{-1}$ (after 1200-time steps), the PbTiO_3 layers are nearly fully downward polarized, producing mostly c/a domain structures (Figure 2d). At this same field, the $\text{Pb}_{0.3}\text{Sr}_{0.7}\text{TiO}_3$ layers also undergo polarization rotation from the in-plane to the out-of-plane direction to produce a largely c -domain structure with minority areas of a domains which extend from the newly formed a domains in the PbTiO_3 layers. Finally, at $E_3 = 1000 \text{ kV cm}^{-1}$ (after 2000-time steps), the structure has nearly completely transformed into a c -domain structure with small minority a domains (Figure 2e). Upon gradually removing the applied field, a reversible back-switching process takes place wherein the system follows the reverse transition path of that just described; thus explaining the antiferroelectric-like switching behavior (Figures S14 and S15, Supporting Information).

This polarization rotation from the in-plane to the out-of-plane direction under electric field is unlike what is typically seen in elastically constrained films and more analogous to that observed in bulk versions of near-morphotropic phase boundary^[23] or relaxor ferroelectrics.^[24] In turn, this warrants investigation of the electromechanical response of this highly responsive system that was accomplished using laser Doppler vibrometry (Experimental Section).^[25] Beginning with $x = 0$, $p = 5$ superlattices, as a reference, small electromechanical responses (0.1% strain at 1000 kV cm^{-1}) are found, but as x is increased, so does the electromechanical response ($>1\%$ strain at 1000 kV cm^{-1} is possible; Figure 2f). To understand this evolution, MD simulations were used to explore the polarization of the system at the unit-cell level (Figures S16–S19, Supporting Information). Using $x = 0.3$ superlattices (Figure 2g) as a model system wherein the ground-state exhibits vortices in PbTiO_3 and in-plane domains in the $\text{Pb}_{0.3}\text{Sr}_{0.7}\text{TiO}_3$ layers, the starting state is such that the majority of the area across the interface has matching in-plane polarization (Figure 2h). Upon increasing the field to $E_1 = 1000 \text{ kV cm}^{-1}$ applied along the $[001]_{\text{pc}}$, regions within the vortices having polarization lying along the $[001]_{\text{pc}}$ expand and the $\text{Pb}_{0.3}\text{Sr}_{0.7}\text{TiO}_3$ layer undergoes polarization rotation; essentially converting to c domains (Figure 2i). The out-of-plane polarized $\text{Pb}_{0.3}\text{Sr}_{0.7}\text{TiO}_3$ facilitates polarization alignment in the PbTiO_3 by mitigating the depolarization effect at the interface (Figure 2j). This explains the augmented response of the $x = 0.3$ and 0.5 superlattices as compared to that of the $x = 0$ superlattices (Figure S16, Supporting Information), where the SrTiO_3 layer is largely unresponsive (i.e., can only be marginally polarized) and thus suppresses the overall electromechanical response. For $x = 0.6$ superlattices (Figure S19, Supporting Information), the MD simulations suggest that the system has a fully c/a -domain structure in the ground state, but unlike single-layer films in the same do-

main structures, these superlattices undergo extensive polarization rotation and overcome the elastic energy costs by lowering the depolarization fields on the PbTiO_3 layer in the fully poled state (Figure S20, Supporting Information). In summary, these switching studies, supported by simulations, explain the intricate mechanism behind the out-of-plane vortex switching and resultant enhanced electromechanical response in all-ferroelectric heterostructures.

Having established that there is considerably increased susceptibility in the out-of-plane direction, the presence of in-plane polarized domains in the $\text{Pb}_x\text{Sr}_{1-x}\text{TiO}_3$ layers also begs the question as to the extent of in-plane responsiveness. To investigate the in-plane switching behavior, interdigitated electrodes (IDE) were fabricated (Experimental Section) such that electric fields can be applied along the $[100]_{\text{pc}}$ (Figure 3a). For $x = 0$ trilayers (Figure 3b), the observed polarization-electric field hysteresis loops (Figure S21, Supporting Information and Experimental Section) are similar to that of other in-plane-polarized ferroelectrics.^[19] Similar hysteresis loops were also observed for $x = 0.3$ trilayers (Figure 3c), but with an increased value of switched polarization and coercivity. In this case, both the vortices in the PbTiO_3 layer and the in-plane oriented domains in the $\text{Pb}_{0.3}\text{Sr}_{0.7}\text{TiO}_3$ layers contribute to the switched polarization (thus giving a larger overall value). In the $\text{Pb}_x\text{Sr}_{1-x}\text{TiO}_3$ system,^[19] the coercivity also increases with x and this, coupled with the polarization and lattice coupling across the interface between the in-plane component of the vortices, contributes to the observed increased coercivity of the trilayers. Overall, the chemistry x provides a deterministic tuning parameter for the switched polarization and coercive field (Figure 3d) for the trilayers (Figure S22, Supporting Information).

To understand how the complex polarization architecture (i.e., a mixture of vortices and in-plane polarized domains) in the all-ferroelectric trilayers switch, phase-field simulations were conducted for $x = 0.3$ trilayers starting from the initial reference state (Figure 3e), under applied fields through an intermediate state (Figure 3f), and finally reaching the switched state (Figure 3g). 3D illustrations depicting the P_x component (Figure 3e–g-i) of the $\text{Pb}_{0.3}\text{Sr}_{0.7}\text{TiO}_3$ and the P_z components (Figure 3e–g-ii) of the PbTiO_3 are provided. In the zero-field, initial state, the net in-plane component of the vortices and the polarization of the $\text{Pb}_{0.3}\text{Sr}_{0.7}\text{TiO}_3$ layers are all aligned along the $[100]_{\text{pc}}$ (Figure 3e). The $\text{Pb}_{0.3}\text{Sr}_{0.7}\text{TiO}_3$ layers consists of a_{1+} and a_{2+} domains (Figure 3e-i). The P_x and P_y components for the PbTiO_3 layer (Figures S23 and S24, Supporting Information) align in an attempt to match with the stripe domains in the $\text{Pb}_{0.3}\text{Sr}_{0.7}\text{TiO}_3$ layers (Figure 3e-i), resulting in a herring-bone-like arrangement of the vortices (Figure 3e-ii). Applying an electric field along the $[100]_{\text{pc}}$ causes the vortex cores to start moving vertically toward the middle of the PbTiO_3 layer and the $\text{Pb}_{0.3}\text{Sr}_{0.7}\text{TiO}_3$ layers see the initial formation of $[100]_{\text{pc}}$ -oriented regions at the outer periphery of the vortices which had polarization along the $[100]_{\text{pc}}$ in the initial state (Figure 3f). The $\text{Pb}_{0.3}\text{Sr}_{0.7}\text{TiO}_3$ layers undergo multiple local switching events^[19] to produce this intermediate state (Figure 3f-i). Again, the vortices adjust to align with the $\text{Pb}_{0.3}\text{Sr}_{0.7}\text{TiO}_3$ -stripe directions, leading to a transient wavy configuration (Figure 3f-ii). Upon further increasing the applied field, both layers complete the switching process by aligning the in-plane component along the $[100]_{\text{pc}}$ (Figure 3g) with the

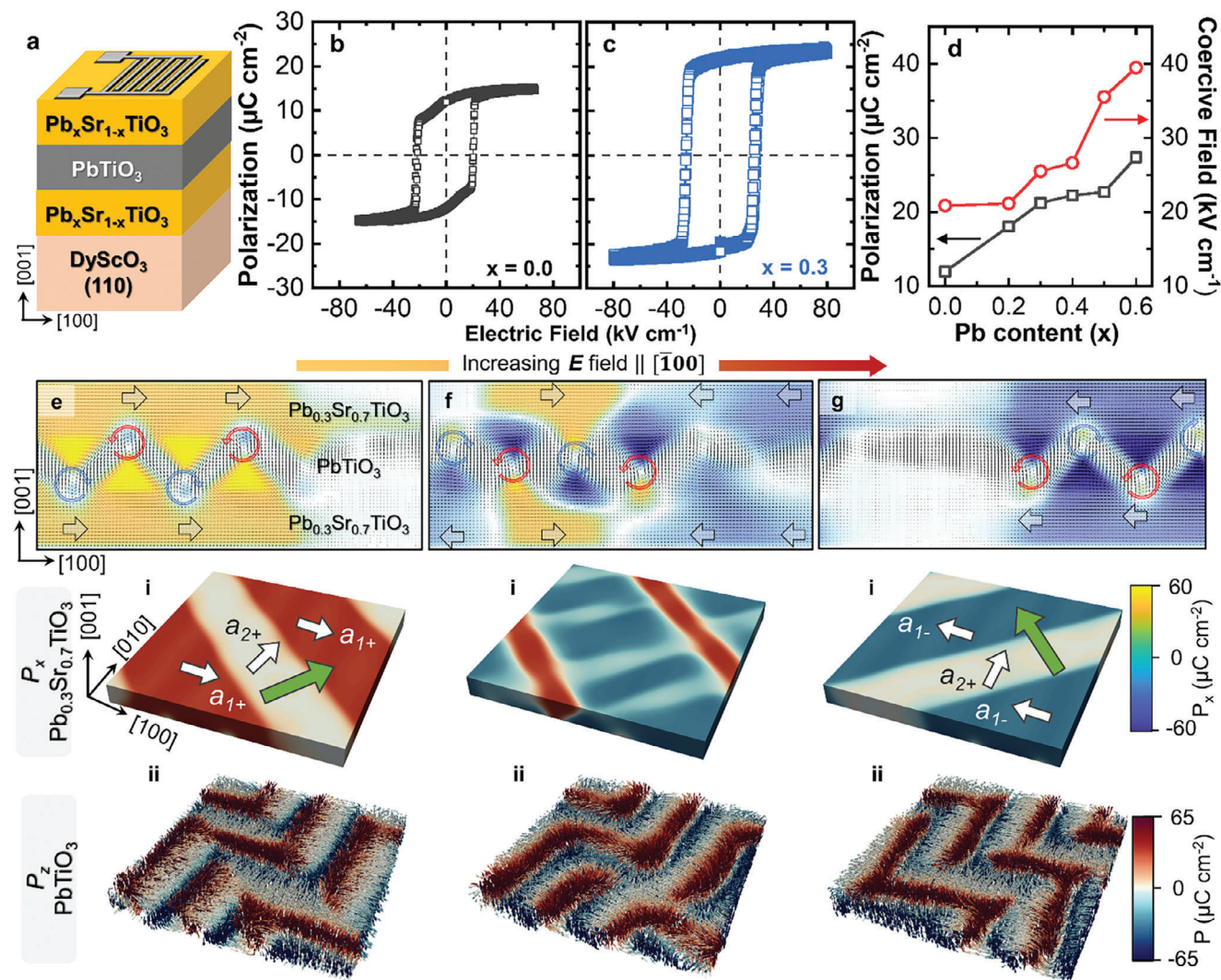


Figure 3. a) Schematic of interdigitated electrodes (IDE) on the trilayer structures. In-plane polarization-electric field hysteresis loops measured at 1 kHz for the b) $x = 0$ and c) $x = 0.3$ trilayers. d) Remanent polarization and coercivity field of the trilayers as a function of lead content (x) in the $\text{Pb}_x\text{Sr}_{1-x}\text{TiO}_3$ layer. Cross-section views of various switching steps for the $x = 0.3$ trilayers extracted from phase-field simulations including e) the initial state, f) intermediate state, and g) final state after completing switching process. Corresponding 3D views of the mesoscale equilibrium domain structures of the trilayer system showing the e–g), i) P_x component of the top $\text{Pb}_{0.3}\text{Sr}_{0.7}\text{TiO}_3$ layer, and the e)–g), ii) P_z component of the PbTiO_3 layer at each switching step.

$\text{Pb}_{0.3}\text{Sr}_{0.7}\text{TiO}_3$ layers regaining a local a_{1-} and a_{2+} variant configuration (Figure 3g-i) and the PbTiO_3 layer having vortices with an in-plane component that matches that of each $\text{Pb}_{0.3}\text{Sr}_{0.7}\text{TiO}_3$ domain stripe (Figure 3g-ii). The investigation of the trilayer-switching processes sheds light on the highly interconnected, synchronized switching processes occurring between the vortex and $\text{Pb}_x\text{Sr}_{1-x}\text{TiO}_3$ layers.

These robust, but unique in-plane polarization switching mechanisms for the vortices and the in-plane-polarized domains open the door for creative design of functionality by stacking different fundamental units together. These fundamental units (such as $x = 0$ and $x = 0.3$ trilayers) have distinct coercive fields and switched polarization values. To demonstrate this potential, $x = 0.3/0$ multilayers were produced with various thicknesses of the shared SrTiO_3 dielectric layer (Figure 4a). For brevity, focus

is given to one variant of this $x = 0.3/0$ multilayer with a SrTiO_3 thickness of 50-unit cells. For this multilayer, two distinct peaks were observed in RSMs (Figure S25, Supporting Information), consistent with a periodicity arising from vortex periodicities of 11.6 and 13.1 nm from the $x = 0$ and $x = 0.3$ trilayers in the stack, respectively, and pointing to their effective structural decoupling with this SrTiO_3 thickness. These two distinct periodicities were captured qualitatively with phase-field simulation with a “thick” shared SrTiO_3 layer (Figure 4b). In the thick SrTiO_3 layer (black dotted box, Figure 4b), a significant portion remains unpolarized, emphasizing the decoupling mechanism.

To probe how these stacked-trilayer structures respond under applied field, in-plane polarization hysteresis loops were measured. Here, the main hysteresis loop (black data, Figure 4c) shows two distinct switching events on each side. The first

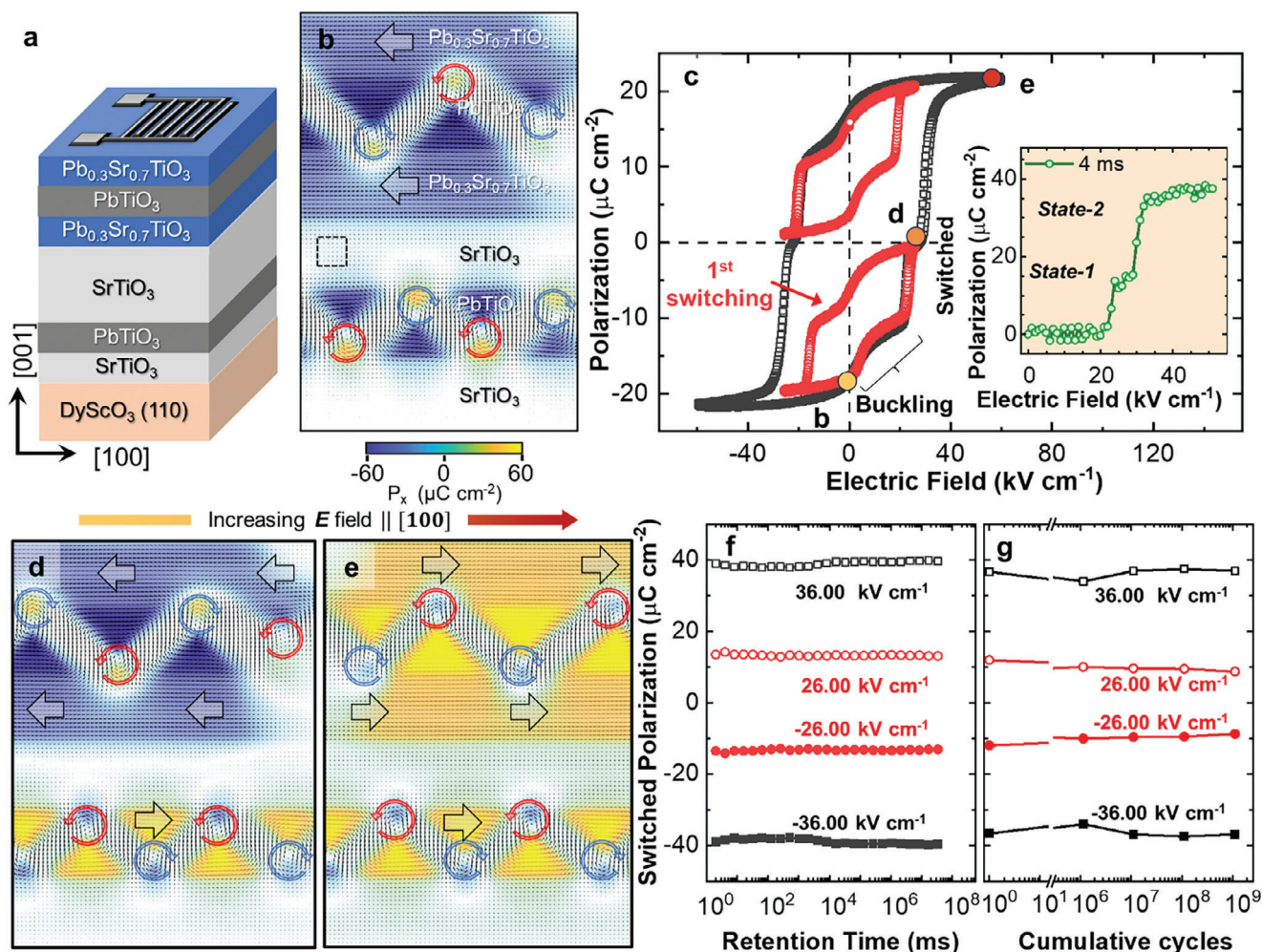


Figure 4. a) Schematic of the $x = 0.3/0$ multilayer with a SrTiO_3 spacer layer of 50-unit cells. b) Cross-sectional view of the phase-field simulations for the same multilayer structure at its ground state. c) In-plane polarization-electric field hysteresis loops measured at 1 kHz for the same multilayer structure wherein the inset shows the positive side of a PUND analysis revealing the multistate character. Cross-sectional phase-field simulations for d) an intermediate switching step and e) the fully switched state. f) The long-term retention of the multiple polarization states and g) the stability of the multiple polarization states after repeated switching cycles.

switching takes place at $\pm 21 \text{ kV cm}^{-1}$ and is referred as the “minor loop” (red data, Figure 4c; Figure S26, Supporting Information) with a switched polarization $\Delta P = 12 \mu\text{C cm}^{-2}$, matching closely with switching characteristics of the $x = 0$ trilayer. A metastable switching event originating from the vertical redistribution of the buckled vortices^[13] is also marked (Figure S27, Supporting Information). Once the applied field exceeds $\pm 28 \text{ kV cm}^{-1}$ the remaining material is switched (resulting in complete switching) with a switched polarization $\Delta P = 22 \mu\text{C cm}^{-2}$, matching closely with switching characteristics of the $x = 0.3$ trilayer. PUND measurements (Inset, Figure 4c; Figure S28, Supporting Information and Experimental Section) reveal a two-step switching process (shown here for positive bias) (Figure S29, Supporting Information), indicative of the multistate switching.

This multi-step-switching process is further illuminated using phase-field simulations. Upon applying E along the $[100]_{\text{pc}}$, the simulations reveal that the first switching event involves only the $x = 0$ trilayer (bottom trilayer, Figure 4d), indicating the struc-

tural decoupling effects on the overall switching process. Further increasing E , the $x = 0.3$ trilayer switches, leading to the second switching event and the complete switching of the multilayer (Figure 4e). The stability of these multistate-switching characteristics was further characterized via retention (Figure S30, Supporting Information and Experimental Section) and fatigue (Figure S31, Supporting Information and Experimental Section) testing for all four states. All four states in these heterostructures were found to be stable and showed minimal change in polarization with time in retention testing over five hours (Figure 4f). Further, it was found that each state could be repeatedly accessed and was easily distinguishable even after $>10^9$ write cycles (Figure 4g). These results indicate several essential features required for robust multistate operation. It is also noted that the multistate nature can be tuned by engineering the thickness of the shared SrTiO_3 layer. For example, data for other cases including a “thin” SrTiO_3 layer thickness (Figures S32–S34, Supporting Information) are shown to produce similar multistate

function while multilayers without a SrTiO₃-separating layer exhibit a single switching event on each side due to strong inter-layer coupling (Figures S35 and S36, Supporting Information). In essence, the shared SrTiO₃ serves as an adjustable parameter by which one can achieve tunable multistate memory in stacked heterostructures.

3. Conclusion

This study showcases the formation of vortices within all-ferroelectric heterostructures. Unlike their cousins in ferroelectric-dielectric heterostructures, these emergent vortices demonstrate superior response to applied stimuli, including large out-of-plane electromechanical strains and ferroelectric polarization due to the ability to freely and reversibly rotate polarization in all layers. In the in-plane direction, robust polar and lattice coupling across the layers leads to synchronized and complete in-plane switching which can then be tuned to allow for multistate switching by stacking different trilayer structures with controlled SrTiO₃ spacer layer thicknesses, elucidating the role of intra-layer coupling and its implications on structural periodicity and multistate switching behavior. All told, this work provides access to highly responsive emergent dipolar textures and access to new functionality.

4. Experimental Section

Synthesis of Materials Using RHEED-Assisted Pulsed-Laser Deposition: Trilayer, multilayer, and superlattice synthesis were performed according to previous works and were reproduced here for completeness. The trilayer, multilayer, and superlattice heterostructures are based on building blocks of the form (Pb_xSr_{1-x}TiO₃)₁₆/(PbTiO₃)₁₆ with (0 ≤ x ≤ 0.6). All films were grown on DyScO₃ (110) substrates via pulsed-laser deposition. All depositions were performed at a laser fluence of 1.5 J cm⁻² in an on-axis geometry using a KrF excimer laser (248 nm, LPX 300, Coherent). All films were grown from Pb_{1.2}TiO₃ ceramic (K. J. Lesker), SrTiO₃ single-crystal, or Pb_xSr_{1-x}TiO₃ (x = 0.24, 0.36, 0.48, 0.60, 0.72) ceramic (ACI alloys) targets. The 20% excess lead in the Pb_{1.2}TiO₃ and Pb_xSr_{1-x}TiO₃ targets was found to be vital to compensate for the lead loss during the PbTiO₃ and Pb_xSr_{1-x}TiO₃ film growths.^[1] The SrRuO₃ top and bottom electrodes were grown at a heater temperature of 650 °C and a dynamic oxygen pressure of 100 mTorr. The trilayer, multilayer, and/or superlattice heterostructures were grown at a heater temperature of 580 °C and a dynamic oxygen pressure of 100 mTorr. The growth was monitored in situ using reflection high-energy electron diffraction (RHEED) and revealed layer-by-layer growth throughout the growth process. RHEED oscillations were monitored for specular spots along the of the DyScO₃ (110) substrate. Following growth, the samples were cooled in 50 Torr of oxygen to room temperature to promote oxidation.

Determination of Crystal Structure via X-Ray Diffraction: The reciprocal space mapping (RSM) studies were completed using a X-ray diffractometer (copper source, K_{α1} radiation of wavelength of 1.5406 Å; Panalytical, X'pert³ MRD), using a hybrid 2-bounce primary monochromator to generate the incident X-ray beam and a PIXcel3D position-sensitive detector. The RSMs were performed on trilayer, multilayer, and superlattice heterostructure about the 220_O (planar section containing the out-of-plane [220]_O with in-plane [332]_O and [420]_O), 332_O (planar section containing the out-of-plane [332]_O with in-plane [220]_O), and 420_O (planar section containing the out-of-plane [420]_O with in-plane [220]_O, where O refers to orthorhombic indices) diffraction conditions of the DyScO₃ (110) substrate to determine the vortex alignment, lateral vortex periodicity, and in-plane ferroelectric domain periodicity of the Pb_xSr_{1-x}TiO₃ layers with a 1/16-degree receiving slit and a detector with an active length of 2.51° in the 2θ angle. The scanning speed is 0.01° (in ω) and 4 s per step.

Scanning Transmission Electron Microscopy and Ptychography: The cross-sectional samples were prepared from characteristic x = 0.3 trilayers using standard lift-out procedures in a Thermo Fisher Helios G4 UX focused-ion beam. Imaging and diffraction measurements were performed on an aberration-corrected Thermo Fisher Spectra 300 X-CFEG STEM with a probe semi-convergence angle of 30 mrad and accelerating voltage of 300 kV. High-angle annular dark field (HAADF) images were acquired with a probe current of 60 pA, collection angle of 60–200 mrad and a dwell time ranging from 200–500 ns per frame. Twenty frames were collected, registered, and averaged for drift correction.

4D-STEM datasets for ptychographic reconstructions and strain mapping were acquired on an EMPAD detector^[26] with a frame time of 1 ms. The ptychographic datasets were taken with a probe semi-convergence angle of 30 mrad, probe current of 60 pA, and focused 10 nm above the sample. Other experimental parameters include an outer collection angle of 53 mrad, step size of 0.58 Å, and a total dose of ≈10⁶ electrons Å⁻². The maximum likelihood method in the fold-slice package was used as the reconstruction algorithm.^[20,27,28] Critical parameters like convergence angle, defocus, and sample thickness were fine-tuned first using Bayesian optimization.^[29] In the final reconstruction, a total number of 15 slices with a slice thickness of 1 nm was used. Six separate probe modes were used to account for partial coherence of the beam. The presented results were obtained after 5000 iterations with a gradual relaxation of the layer regularization along the beam direction.

The datasets for strain mapping were obtained with the microscope operated in microprobe mode with a probe semi-convergence angle of 2 mrad, collection angle of 34 mrad, and a probe current of 230 pA. The calculation of the strain maps was done using the cepstral algorithm.^[30,31] The cepstral pattern was calculated as the Fourier transform of the logarithm of each diffraction pattern, and the peaks in cepstral space correspond to projected inter-atomic spacings. These peak positions in each cepstral pattern are tracked with sub-pixel precision to calculate the local variations in lattice parameter from which the components of the strain tensor are calculated.

To characterize the dipole moment at the atomic scale, atomic displacements were measured for each pseudo-cubic unit cell of PbTiO₃ and Pb_xSr_{1-x}TiO₃. There are multiple choices one can make for the unit cell – here, the pseudo-cubic unit cell centered at the B-site (titanium) cation was chosen, without loss of generality. A sliding paraboloid with a radius of 300 pixels was used for background subtraction on the ptychographic reconstruction to remove phase ramps and denoise the image. Precise coordinates of all atoms (A- and B-site cations and oxygen for ptychographic images and A- and B-site cations for HAADF images) are measured using a 2D-Gaussian fit around each atom, implemented using the Atomap package.^[32] For each B-site cation, the centroid of the neighboring four A-site cations and the centroid of the neighboring four oxygen anions (information about the other two oxygen atoms are lost in projection as they lie on the same column as the B-site cations) are calculated from the ptychographic image. The vectors connecting the centroid of the oxygen anions to the i) B-site cation and ii) the centroid of the A-site cations, define the two dipole moments present in the system. The measured displacement maps agree with the expected polarization texture from MD and phase-field simulations.

Since HAADF images are insensitive to the light oxygen atoms,^[33] the vector connecting the B-site to the A-site centroid is often used to qualitatively describe the microscopic polarization under the rationale that the dipole manifests as a relative shift of one cation sublattice with respect to the other. This assumption is, however, insufficient for the Pb_xSr_{1-x}TiO₃ layer, where the measurement of oxygen atoms is critical in extracting the correct information about the microscopic dipole moment.

Molecular-Dynamics (MD) Simulations: MD simulations utilized a deep neural network-based force field that was developed for both Pb_xSr_{1-x}TiO₃ solid solutions and (PbTiO₃)_n/(Pb_xSr_{1-x}TiO₃)_n superlattices.^[34] This force field effectively generated the temperature-composition phase diagram for Pb_xSr_{1-x}TiO₃ solid solutions, thereby enabling extension to the (PbTiO₃)_n/(Pb_xSr_{1-x}TiO₃)_n system. A 60 × 20 × 32 supercell consisting of 192 000 atoms was used to model (PbTiO₃)₁₆/(Pb_xSr_{1-x}TiO₃)₁₆ superlattices, and the in-plane lattice

constants were kept the same as experimental substrate values. All MD simulations were performed in the isobaric-isothermal (NPT) ensemble using LAMMPS.^[35] The temperature was maintained at 300 K via the Nosé-Hoover thermostat and the pressure was kept at 1.0 bar by the Parrinello-Rahman barostat. The timestep was set to 2 fs. For all simulations, the equilibrium run was 20 ps followed by a production run of 80 ps.

Out-Of-Plane Device Fabrication: The electrical properties for all the superlattices were studied with symmetric 30-nm-thick SrRuO₃ films serving as the top and bottom electrodes. Following the growth of the desired heterostructures, capacitor structures were fabricated via photolithography and wet etching. A photoresist layer (OCG 825 35CS, FUJIFILM Electronic Materials) was spin-coated on the heterostructures using a spin-coater (KW-4A, Chemat Technology) with a spin speed of 1000 rpm for 10 s, followed by 6000 rpm for 40 s. The heterostructures were then soft-baked at 95 °C for 120 s using a hot plate (KW-4AH, Chemat Technology). Next, the heterostructures were exposed to ultraviolet light through a photomask in a mask-alignment system (Hybrid Technology Group, Inc.) for 120 s. After the exposure, the heterostructures were developed in a 1:1 water and Microposit developer concentrate (Rohm and Haas Electronic Materials LLC) for 40 s. The samples were then washed thoroughly with water to remove any remaining developer solution on sample. The top SrRuO₃ layer was then selectively wet-etched by an NaIO₄ aqueous solution (0.1 mol L⁻¹) to realize circular capacitor array of circles with diameters of 25 μm and 50 μm.

Out-Of-Plane Hysteresis Loop Measurements: The electrical properties for all superlattices were studied with circular capacitor structures (diameter of 25 μm) patterned from the top 30-nm-thick SrRuO₃ electrode. To contact the sample electrodes, tungsten probe tips (model 7-B, The Micromanipulator Company) with a point radius of 0.5 μm were used. The polarization as a function of electric field (−1000 to 1000 kV cm⁻¹) for these circular capacitor structures was measured at room temperature using a Precision Multiferroic Tester (Radiant Technologies, Inc.) with 10 kHz double bipolar waveform.

Phase-Field Simulations: Phase-field simulations were used to simulate the temporal evolution of polarization in (PbTiO₃)₁₆/(Pb_xSr_{1-x}TiO₃)₁₆ (0 ≤ x ≤ 0.6)-based trilayers, multilayers, and superlattices. In the phase-field model, the time evolution of the polarization field is described by the time-dependent Ginzburg-Landau equation (TDGL):

$$\frac{\partial P_i(r_i, t)}{\partial t} = -L \frac{\delta F}{\delta P_i(r_i, t)} \quad (1)$$

where P_i represents the spontaneous polarization (measured in C m⁻²), r_i represents the position in space, t is time, and L is the kinetic coefficient relating to the rate of polarization relaxation or the speed of domain-wall motion. The total free energy functional (F) contains the following energy-density terms.

$$F = \int (f_{\text{Landau}} + f_{\text{Elastic}} + f_{\text{Electric}} + f_{\text{Gradient}}) dV \quad (2)$$

Following the Landau-Devonshire theory of ferroelectrics, f_{Landau} is the Landau free energy of the Pb_xSr_{1-x}TiO₃ (PSTO) system and it is described by a sixth-order polynomial expansion of the polarization order parameter:

$$\begin{aligned} f_{\text{Landau}}(P_i) = & \alpha_1 (P_1^2 + P_2^2 + P_3^2) + \alpha_{11} (P_1^4 + P_2^4 + P_3^4) \\ & + \alpha_{12} (P_1^2 P_2^2 + P_1^2 P_3^2 + P_2^2 P_3^2) + \alpha_{111} (P_1^6 + P_2^6 + P_3^6) \\ & + \alpha_{112} (P_1^4 (P_2^2 + P_3^2) + P_2^4 (P_1^2 + P_3^2) \\ & + P_3^4 (P_2^2 + P_1^2)) + \alpha_{123} P_1^2 P_2^2 P_3^2 \end{aligned} \quad (3)$$

where α_i , α_{ij} , and α_{ijk} are the dielectric stiffness coefficients measured under constant stress. For Pb_xSr_{1-x}TiO₃, the coefficients were obtained from

fitting to experimental dielectric and phase transition data.^[36] The Landau energy coefficients are:

$$a_1 (C^{-2} m^2 N) = \frac{T_s}{2\epsilon_0 C} \left(\text{Coth} \left(\frac{T_s}{T} \right) - \text{Coth} \left(\frac{T_s}{T_c} \right) \right) \quad (4)$$

where C (K⁻¹ × 10⁵) = 1.50 − 0.995(1 − x)^{2.77} is the Curie-Weiss constant, T_c (K) = 752 − 697(1 − x) is the critical temperature, and T_s (K) = 54 is the saturation temperature, below which quantum fluctuations begin to play an important role. The other Landau coefficients are a_{11} (C⁻⁴ m⁶ N) = (17.73(1 − x)^{3.2} + 0.73) × 10⁸, a_{12} (C⁻⁴ m⁶ N) = (24(1 − x)^{1.5} + 7.5) × 10⁸, a_{111} (C⁻⁶ m¹⁰ N) = (20(1 − x) + 2.6x) × 10⁸, a_{112} (C⁻⁶ m¹⁰ N) = (8(1 − x) + 6.1x) × 10⁸, a_{123} (C⁻⁶ m¹⁰ N) = (−3.7x + 20(1 − x)) × 10⁹. In all equations, x denotes the amount of PbTiO₃ in the system. For the pure SrTiO₃ spacer layer, a 4th order expansion was used. The Landau energy coefficients are a_1 (C⁻² m² N) = 4.05 × 10⁷ (Coth($\frac{54}{T}$) − Coth($\frac{54}{30}$)), a_{11} (C⁻⁴ m⁶ N) = 17.0 × 10⁸, a_{12} (C⁻⁴ m⁶ N) = 13.7 × 10⁸.^[36]

The elastic energy density is:

$$f_{\text{Elastic}} = c_{ijkl} (\epsilon_{ij} - \epsilon_{ij}^0) (\epsilon_{kl} - \epsilon_{kl}^0) \quad (5)$$

$$\epsilon_{ij}^0 = Q_{ijkl} P_k P_l \quad (6)$$

where c_{ijkl} is the elastic stiffness tensor, Q_{ijkl} is the electrostrictive tensor, ϵ_{ij} is the total strain, and ϵ_{ij}^0 is the stress-free strain (or eigenstrain) which is related to the magnitude of the polarization. The electrostrictive coefficients are Q_{11} (m⁴ C⁻² × 10⁻²) = 8.9 − 3.81(1 − x)⁵, Q_{12} (m⁴ C⁻² × 10⁻²) = −1.31(1 − x) − 2.6x, Q_{44} (m⁴ C⁻² × 10⁻²) = 1.065(1 − x) + 6.75x, and the elastic compliance tensor is given by S_{11} (m²/N) = 8.0 × 10⁻¹²(1 − x) + 3.52 × 10⁻¹²x, S_{12} (m²/N) = −2.5 × 10⁻¹²(1 − x) − 0.85 × 10⁻¹²x, and S_{44} (m²/N) = 9.0 × 10⁻¹²x + 7.87 × 10⁻¹²(1 − x).

The electrostatic-energy density is given by:

$$f_{\text{Electric}} = -\frac{1}{2} \kappa_0 \kappa_{ij}^b E_i E_j - E_i P_i \quad (7)$$

where κ_0 is the vacuum permittivity and κ_{ij}^b is the background dielectric constant which is chosen as 45 and to be isotropic. For the in plane switching simulations, a uniform electric field was applied along the [100]_{pc} ranging from −120 kV cm⁻¹ to 120. For the out-of-plane switching simulations, a uniform electric-field was applied along the [001]_{pc} ranging from −1000 to 1000 kV cm⁻¹. Further information on solving the elastic and electrostatic equilibrium with equations with large elastic and dielectric inhomogeneity can be found in the literature.^[37]

The local gradient energy contribution can be defined as,

$$f_{\text{Gradient}} = \frac{1}{2} G_{ijkl} \frac{\partial P_i}{\partial x_j} \frac{\partial P_k}{\partial x_l} \quad (8)$$

where an isotropic gradient-energy tensor was assumed, G_{ijkl} , with renormalized values of $G_{11} = 0.60$, $G_{12} = -0.60$, and $G_{44} = 0.60$ in Voigt notation.

For all simulations a system size of (128Δx₁ × 128Δx₂ × (h + 24)Δx₃) was used. Here, h represents the thickness of the film with $h\Delta x_3$ grid points as the ferroelectric multilayer film, there are 20Δx₃ grid points as the substrate, the elastic constants are assumed to be the same as the film, and there are 4Δx₃ grid points acting as a vacuum layer above the film. Periodic boundary conditions were applied for the in-plane lateral directions, whereas natural boundary conditions were applied to the film-vacuum and film-substrate interfaces. In all simulations Δx₁ = Δx₂ = Δx₃ = 0.4 nm.

The multilayer structure is defined by spatially varying the material properties (i.e., the Landau coefficients, elastic stiffness, etc.) using a sharp interface description. The interface between the film and substrate is assumed to be coherent. Therefore, the lattice mismatch strains between

the DyScO₃ (110) (DSO) substrate and the ferroelectric layers were calculated using the equivalent cubic lattice constant ($a_{\text{PbTiO}_3}^{\text{PC}} = 3.9569 \text{ \AA}$, $a_{\text{SrTiO}_3}^{\text{PC}} = 3.905 \text{ \AA}$, $a_{\text{Pb}_{0.3}\text{Sr}_{0.7}\text{TiO}_3}^{\text{PC}} = 3.9128 \text{ \AA}$) and the pseudocubic lattice parameters of DSO ($0.5\sqrt{a^2 + b^2} = 3.946 \text{ \AA}$, $0.5c = 3.952$).^[38] Since the lattices of the film and substrate are orthogonal, there is no in-plane shear misfit strain such that:

$$\epsilon_{11} = \frac{a_{\text{DSO}}^{[100]} - a_{\text{Ferroelectric}}^{\text{PC}}}{a_{\text{DSO}}^{[100]}}, \quad \epsilon_{22} = \frac{a_{\text{DSO}}^{[010]} - a_{\text{Ferroelectric}}^{\text{PC}}}{a_{\text{DSO}}^{[010]}}, \quad \epsilon_{12} = \epsilon_{21} = 0 \quad (9)$$

To initiate the simulation, random noise was applied to each spatial vector point, and the simulation evolved to a steady-state condition. Next, the electric field was applied to simulate the switching behaviors with the electric field E changing by 250 V m^{-1} for each time step for the in-plane switching simulations and 5000 V m^{-1} per time step for the out of plane switching simulations. All phase-field simulations were completed using the μPro software.

Electromechanical Response Measurements: To study the electromechanical response of the superlattice heterostructures, a non-contact single-beam laser Doppler vibrometer (VibroOne, PolyTech GmbH) integrated with a Precision Ferroelectric Tester (Radiant Technologies) was employed. A $1.5\text{-}\mu\text{m}$ -diameter laser spot (HeNe laser with a wavelength of 633 nm) was focused vertically on the top surface of the capacitor structure. To contact the sample electrodes, tungsten probe tips (model 7-A, The Micromanipulator Company) with a point radius of $0.35 \text{ }\mu\text{m}$ were used. A triangular electric field wave with a frequency of 3 kHz was applied across the capacitor, and the resulting electromechanical response (i.e., the surface displacement) of the superlattices were measured by the Doppler shift of the backscattered laser beam, with a sensitivity of $\approx 2 \text{ pm}$. The electromechanical strain value was defined as the ratio of the surface displacement to the thickness of the superlattice films, which was calculated as the average of values in 25 repeated measurements. During the measurement, the superlattices were glued on a rigid glass substrate, and the electrode areas were as small as $50 \text{ }\mu\text{m}$, so as to minimize the potential for substrate bending that may contribute to the measured response.

Probing Electromechanical Response via MD Simulations: After reaching equilibrium under zero-field conditions, an electric field evolving from 100 to 1000 kV cm^{-1} was applied to the superlattice. Subsequently, the newly equilibrated lattice constants were derived through the MD simulations, enabling the calculation of the electromechanical response of the superlattices. The interaction between the electric field and each atom was calculated by multiplying the electric-field strength by the Born effective charge (BEC) of the respective atom. These BEC values were computed utilizing density-functional theory (DFT). All DFT calculations were executed using the Vienna Ab initio Simulation Package (VASP),^[39,40] employing the projected augmented wave method.^[41,42] The Perdew-Burke-Ernzerhof functional modified for solids (PBEsol),^[43] within the framework of the generalized gradient approximation, was employed as the exchange-correlation functional, with an energy cutoff of 800 eV and a k -point spacing of 0.3 \AA^{-1} . For a given composition, a $2 \times 2 \times 3$ supercell was used, and the averaged BEC value of the A -site cation was determined by averaging the BEC values of all 12 A -site cations. This methodology was similarly applied to the B -site cations and oxygen ions. All the BEC values for various compositions have been tabulated (Table S1, Supporting Information).

In-Plane Device Fabrication: In-plane device structures were patterned via UV lithography using a Heidelberg MLA150 Maskless Aligner in the Berkeley Marvell NanoLab using AZ MiR 701 Photoresist. For these devices, interdigitated electrodes (IDE) with finger length $120 \text{ }\mu\text{m}$ and finger spacing $5 \text{ }\mu\text{m}$ were used. After patterning, a layer of $\approx 5 \text{ nm}$ of titanium (which is used as an adhesion layer) and a layer of $\approx 80 \text{ nm}$ of platinum was deposited at room temperature via DC magnetron sputtering with base pressure of $\approx 10^{-8} \text{ Torr}$. Titanium and platinum were sputtered at 20 and 15 W , respectively, in argon pressures of 3.3 and 7.0 mTorr resulting in growth rates of 1.7 and 8.7 nm min^{-1} , respectively. The additional metal

deposited outside the primary device structure was then lifted off via an $\approx 5\text{-h}$ soak in 1-methyl-2-pyrrolidone (NMP) at $85 \text{ }^\circ\text{C}$ that was maintained using a hot plate (Thermo Scientific HP88854100 Cimarec+ Digital Hot-plate).

In-Plane Ferroelectric Hysteresis Loop Measurements: Polarization-electric field hysteresis loops were measured using a Precision Multiferroic Tester (Radiant Technologies, Inc.). The hysteresis loop measurements were performed at 1 kHz with a double bipolar waveform at an amplitude varying from 10 to 50 V , depending on the measurement requirements. To contact the sample electrodes, tungsten probe tips (model 7-B, The Micromanipulator Company) with a tip radius of $0.5 \text{ }\mu\text{m}$ were used. Polarization-electric field hysteresis loops were captured for a given sample using in-plane interdigitated electrodes (IDE) platinum devices. Due to the device geometry, the hysteresis loops included a ferroelectric switching signal and a dielectric background signal (Figure S21a, Supporting Information). Linear fitting was done at both ends at the high-field region (positive and negative), where the signal predominantly comes from the dielectric background (Figure S21a, Supporting Information). The equation of a single line was then calculated (Figure S21b, Supporting Information) by taking an average of the slope and linear intercept of the previously assessed two linearly fitted lines at the high-field regions (positive and negative). This linear equation was then subtracted from the raw hysteresis loop data to get the actual switched polarization (Figure S21c, Supporting Information).

To capture the minor hysteresis loop associated with the first switching event on the positive side of the loop, first, a double bipolar waveform with voltage amplitude (V_{main}) large enough to switch the whole system was applied (Figure S26a, Supporting Information). This waveform captures all four states related to the entire switching cycle (Figure S26b, Supporting Information). The end state of this bipolar waveform is zero volts, which is approached explicitly from the negative voltage side. This waveform configuration leads all layers of the system to be poled negatively. Next, to capture the minor hysteresis loop switching event on the positive side of the hysteresis loop, a similar waveform, but this time with just enough voltage to switch the first switching event (V_{minor}) is applied in the bipolar waveform (Figure S26c, Supporting Information). Again, this waveform should start from zero volts and rise to the voltage amplitude of V_{minor} in the positive direction in the first quadrant. This waveform will apply just enough voltage to switch the layers responsible for the first switching event of the system from the fully negatively poled initial state (Figure S26d, Supporting Information). This minor loop can then be adjusted vertically to match the first switching event of the major loop captured initially (Figure S26e, Supporting Information).

To capture the buckling loop,^[13] associated with the first switching event on the positive side of the loop, first, a double bipolar waveform with voltage amplitude (V_{main}) large enough to switch whole system was applied as shown (Figure S27a, Supporting Information). This waveform captures all four states related to the entire switching cycle (Figure S27b, Supporting Information). The end state of this bipolar waveform is zero volts, which is approached explicitly from the negative voltage side. This waveform configuration leads all layers of the system to be poled negatively. Next, to capture the buckling loop switching event on the positive side of the hysteresis loop, a similar waveform, but this time just enough to capture buckling phenomenon (V_{buckling}) was applied in the bipolar waveform as shown (Figure S27c, Supporting Information). Again, this waveform should start from zero volts and rise to the voltage amplitude of V_{buckling} in the positive direction in the first quadrant. This waveform will apply just enough voltage to induce the buckling-switching event of the system from the fully negatively poled initial state (Figure S27d, Supporting Information). This buckling loop can then be adjusted vertically to match the first switching event of the major loop captured initially (Figure S27e, Supporting Information).

Positive-Up-Negative-Down (PUND) Measurements: Pulsed-switching measurements were performed using a PUND-pulse sequence on the in-plane device structures using a Precision Multiferroic Tester (Radiant Technologies, Inc.). PUND tests were used to study the multistate switching behavior of the multilayer heterostructures. A conventional PUND pulse sequence was used in these measurements (Figure S28, Supporting

Information). Each measurement cycle is made up of five pulses comprising one preset pulse and four reading pulses with specific voltages and widths. A large preset voltage was applied at the beginning of each cycle to pre-pole the in-plane domain architecture in the negative-voltage direction; no measurement was performed for this pulse. The pulse width was kept constant ($t = 1$ ms and 4 ms in this work), while the pulse voltage was increased by 0.5 V for each consecutive cycle. The second pulse switches the in-plane domains to the positive-voltage direction and measures the amount of switched polarization. The third pulse was an exact replica of the second pulse, which was used to read the non-remnant part of polarization along with the dielectric background, which dissipates during the delay time after the second pulse. The fourth and fifth pulses mirror the second and third, and switch the capacitor to the negative-voltage direction and read both the switched and non-switched polarization, respectively. The delay time between all the pulses was set to $t = 100$ ms to let the in-plane domain structures backswitch (if required). These measurements produce values for $\pm P^*$, $\pm P_r^*$, $\pm P^*$, and $\pm P_r^*$ and $\Delta P = P^* - P^*$, $\Delta P_r = P_r^* - P_r^*$, $-\Delta P = -P^* - (-P^*)$ and $-\Delta P_r = -P_r^* - (-P_r^*)$. Here, the asterisk (*) represents the total of remanent and non-remnant polarization components and r represents the remanent polarization component only. $+P^*$ ($-P^*$) is measured at the end of the second (fourth) pulse when the voltage is on, and $+P_r^*$ ($-P_r^*$) is measured after a certain amount of delay time (100 ms) when the voltage is off after the second (fourth) pulse. $+P^*$ ($-P^*$) is measured at the end of the third (fifth) pulse when the voltage is on, and $+P_r^*$ ($-P_r^*$) was measured after a certain amount of delay time (100 ms) when the voltage is off after the third (fifth) pulse. These four terms (ΔP , $-\Delta P$, ΔP_r , $-\Delta P_r$) defined here are four different calculations of the remanent polarization only and have produced very similar results.

Retention Measurements: The retention measurements were performed using a Precision Multiferroic Tester (Radiant Technologies, Inc.). Like the PUND measurements, a large preset voltage (here, -50 V applied for 1 ms) was applied at the beginning of each cycle to pre-pole the in-plane domain structures to negative-voltage direction; no measurement was performed for this pulse (Figure S30, Supporting Information). Each polarization state was first accessed using an appropriate pulse width and voltage which were extracted from the previously shown PUND measurements. For example, 13 V and 1 ms for the partly switched intermediate state (state 1) on the positive side of the hysteresis loop of $x = 0.3/0$ multilayers with a SrTiO₃ spacer layer of 50-unit cells, and 18 V and 1 ms for the completely switched state (state 2). The system was then held at zero voltage for a specific retention time. In this case, starting with 2 ms retention time and then doubling for each successive cycle. After each writing cycle and the retention wait period, a reading pulse and non-switching pulse (-40 V and 1 ms) was subsequently applied to analyze the retention behavior of the switched polarization. A similar process was repeated on the negative side to get characteristics of the retention behavior on the negative side of the switched polarization.

Fatigue Measurements: The fatigue measurements were performed using a Precision Multiferroic Tester (Radiant Technologies, Inc.). The fatigue measurement pulse sequence consists of a large number of triangular waveforms with a voltage amplitude large enough to completely switch the multilayer systems at 1 MHz, followed by the PUND measurement (Figure S31, Supporting Information). In this measurement, the fatigue cycles were applied to the in-plane device to switch the in-plane domains as many as 1.1×10^9 cycles. The fatigue cycles were interrupted regularly by PUND measurement pulses, which monitor the variation of the remanent polarization as a function of write cycles with the known combination of pulse voltage and width. For example, 13 V and 1 ms for state 1 on the positive side of the hysteresis loop of $x = 0.3/0$ multilayers with a SrTiO₃ spacer layer of 50-unit cells, and 18 V and 1 ms for the completely switched state 2 to imitate the writing of various multistate polarization values after a large number of fatigue cycles. Consequently, these measurements produce $\pm P^*$, $\pm P_r^*$, $\pm P^*$, and $\pm P_r^*$ and $\Delta P = P^* - P^*$, $\Delta P_r = P_r^* - P_r^*$, $-\Delta P = -P^* - (-P^*)$, and $-\Delta P_r = -P_r^* - (-P_r^*)$ as explained previously in the section on the PUND measurements. These four terms (ΔP , $-\Delta P$, ΔP_r , $-\Delta P_r$) defined here are four different calculations of the remanent polarization only and have again produced very similar results.

Supporting Information

Supporting Information is available from the Wiley Online Library or from the author.

Acknowledgements

P.K., A.M.R., H.K., P.M., P.B., and J.A.Z. acknowledge the support of the Army Research Office under the ETHOS MURI via cooperative agreement W911NF-21-2-0162. A.M.R. acknowledges the support of the National Science Foundation Graduate Research Fellowship Program under Grant No. DGE1255832. The phase-field simulations in this work were performed using Bridges-2 at the Pittsburgh Supercomputing Center through allocation MAT230041 from the ACCESS program, which is supported by National Science Foundation grants #2138259, #2138286, #2138307, #2137603, and #2138296. A.D. acknowledges the support of the National Science Foundation under Grant DMR-2102895. J.Y. and S.L. acknowledge the support of Natural Science Foundation of Zhejiang Province Award Number 2022XHSJ006 and Westlake Education Foundation, and the computational resource provided by Westlake High-Performance Computing Center. C.-C.L. acknowledges the support of the Army Research Office under W911NF-21-1-0118 and the Taiwan Major Fields Scholarship from the Ministry of Education in Taiwan. H.P. acknowledges that this research was sponsored by the Army Research Laboratory and was accomplished under Cooperative Agreement Number W911NF-24-2-0100. The views and conclusions contained in this document are those of the authors and should not be interpreted as representing the official policies, either expressed or implied, of the Army Research Laboratory or the U.S. Government. The U.S. Government is authorized to reproduce and distribute reprints for Government purposes notwithstanding any copyright notation herein. X.H. acknowledges the support from SRC-JUMP ASCENT center. S.D. acknowledges Science and Engineering Research Board (SRG/2022/000058 and EEQ/2023/000089) and Indian Institute of Science start up grant for financial support. Y.-T.S. acknowledges support from the USC Viterbi startup funding and the USC Research and Innovation Instrumentation Award. H.K. and D.A.M. acknowledge the use of electron microscopy studies supported by the Cornell University Materials Research Science and Engineering Center (NSF DMR-1719875, DMR-1539918) and the Platform for the Accelerated Realization, Analysis, and Discovery of Interface Materials (NSF DMR-2039380) along with John Grazul, Malcolm Thomas and Mariena Silvestry Ramos for technical support and maintenance of the electron microscopy facilities. L.-Q.C. and L.W.M. acknowledge support from the U.S. Department of Energy, Office of Science, Office of Basic Energy Sciences, under Award Number DE-SC-0012375 for the development of dipolar textures in complex-oxide superlattices.

Conflict of Interest

The authors declare no conflict of interest.

Data Availability Statement

Research data are not shared.

Keywords

dipolar texture, ferroelectric vortices, in-plane ferroelectrics, multistate, thin-film superlattices

Received: July 14, 2024
Revised: October 3, 2024
Published online:

- [1] A. K. Yadav, C. T. Nelson, S. L. Hsu, Z. Hong, J. D. Clarkson, C. M. Schlepütz, A. R. Damodaran, P. Shafer, E. Arenholz, L. R. Dedon, D. Chen, A. Vishwanath, A. M. Minor, L. Q. Chen, J. F. Scott, L. W. Martin, R. Ramesh, *Nature* **2016**, 530, 198.
- [2] F.-H. Gong, Y.-L. Tang, Y.-L. Zhu, H. Zhang, Y.-J. Wang, Y.-T. Chen, Y.-P. Feng, M.-J. Zou, B. Wu, W.-R. Geng, Y. Cao, X.-L. Ma, *Sci. Adv.* **2021**, 7, eabg5503.
- [3] S. Das, Y. L. Tang, Z. Hong, M. A. P. Gonçalves, M. R. McCarter, C. Klewe, K. X. Nguyen, F. Gómez-Ortiz, P. Shafer, E. Arenholz, V. A. Stoica, S. L. Hsu, B. Wang, C. Ophus, J. F. Liu, C. T. Nelson, S. Saremi, B. Prasad, A. B. Mei, D. G. Schlom, J. Íñiguez, P. García-Fernández, D. A. Muller, L. Q. Chen, J. Junquera, L. W. Martin, R. Ramesh, *Nature* **2019**, 568, 368.
- [4] Y. J. Wang, Y. P. Feng, Y. L. Zhu, Y. L. Tang, L. X. Yang, M. J. Zou, W. R. Geng, M. J. Han, X. W. Guo, B. Wu, X. L. Ma, *Nat. Mater.* **2020**, 19, 881.
- [5] J. Junquera, Y. Nahas, S. Prokhorenko, L. Bellaiche, J. Íñiguez, D. G. Schlom, L. Q. Chen, S. Salahuddin, D. A. Muller, L. W. Martin, R. Ramesh, *Rev. Mod. Phys.* **2023**, 95, 25001.
- [6] A. R. Damodaran, J. D. Clarkson, Z. Hong, H. Liu, A. K. Yadav, C. T. Nelson, S. L. Hsu, M. R. McCarter, K. D. Park, V. Kravtsov, A. Farhan, Y. Dong, Z. Cai, H. Zhou, P. Aguado-Puente, P. Garcia-Fernandez, J. Iniguez, J. Junquera, A. Scholl, M. B. Raschke, L. Q. Chen, D. D. Fong, R. Ramesh, L. W. Martin, *Nat. Mater.* **2017**, 16, 1003.
- [7] P. Behera, M. A. May, F. Gómez-Ortiz, S. Susarla, S. Das, C. T. Nelson, L. Caretta, S. L. Hsu, M. R. McCarter, B. H. Savitzky, E. S. Barnard, A. Raja, Z. Hong, P. García-Fernandez, S. W. Lovesey, G. van der Laan, P. Ercius, C. Ophus, L. W. Martin, J. Junquera, M. B. Raschke, R. Ramesh, *Sci. Adv.* **2022**, 8, 1.
- [8] S. Das, Z. Hong, V. A. Stoica, M. A. P. Gonçalves, Y. T. Shao, E. Parsonnet, E. J. Marksz, S. Saremi, M. R. McCarter, A. Reynoso, C. J. Long, A. M. Hagerstrom, D. Meyers, V. Ravi, B. Prasad, H. Zhou, Z. Zhang, H. Wen, F. Gómez-Ortiz, P. García-Fernández, J. Bokor, J. Íñiguez, J. W. Freeland, N. D. Orloff, J. Junquera, L. Q. Chen, S. Salahuddin, D. A. Muller, L. W. Martin, R. Ramesh, *Nat. Mater.* **2021**, 20, 194.
- [9] A. K. Yadav, K. X. Nguyen, Z. Hong, P. García-Fernández, P. Aguado-Puente, C. T. Nelson, S. Das, B. Prasad, D. Kwon, S. Cheema, A. I. Khan, C. Hu, J. Íñiguez, J. Junquera, L. Q. Chen, D. A. Muller, R. Ramesh, S. Salahuddin, *Nature* **2019**, 565, 468.
- [10] V. A. Stoica, N. Laanait, C. Dai, Z. Hong, Y. Yuan, Z. Zhang, S. Lei, M. R. McCarter, A. Yadav, A. R. Damodaran, S. Das, G. A. Stone, J. Karapetrova, D. A. Walko, X. Zhang, L. W. Martin, R. Ramesh, L. Q. Chen, H. Wen, V. Gopalan, J. W. Freeland, *Nat. Mater.* **2019**, 18, 377.
- [11] Q. Li, V. A. Stoica, M. Paściak, Y. Zhu, Y. Yuan, T. Yang, M. R. McCarter, S. Das, A. K. Yadav, S. Park, C. Dai, H. J. Lee, Y. Ahn, S. D. Marks, S. Yu, C. Kadlec, T. Sato, M. C. Hoffmann, M. Chollet, M. E. Kozina, S. Nelson, D. Zhu, D. A. Walko, A. M. Lindenberg, P. G. Evans, L. Q. Chen, R. Ramesh, L. W. Martin, V. Gopalan, J. W. Freeland, et al., *Nature* **2021**, 592, 376.
- [12] P. Behera, A. M. Ross, N. Shanker, P. Meisenheimer, M. Manna, S.-L. Hsu, P. Kavle, I. Harris, S. Husain, A. Raja, L. W. Martin, S. Susarla, S. Salahuddin, L.-Q. Chen, R. Ramesh, *Adv. Mater.* **2023**, 35, 2208367.
- [13] P. Behera, E. Parsonnet, F. Gómez-Ortiz, V. Srikrishna, P. Meisenheimer, S. Susarla, P. Kavle, L. Caretta, Y. Wu, Z. Tian, A. Fernandez, L. W. Martin, S. Das, J. Junquera, Z. Hong, R. Ramesh, *Adv. Mater.* **2023**, 35, 2208367.
- [14] D. Rusu, J. J. P. Peters, T. P. A. Hase, J. A. Gott, G. A. A. Nisbet, J. Stremper, D. Haskel, S. D. Seddon, R. Beanland, A. M. Sanchez, M. Alexe, *Nature* **2022**, 602, 240.
- [15] M. Hadjimichael, Y. Li, E. Zatterin, G. A. Chahine, M. Conroy, K. Moore, E. N. O. Connell, P. Ondrejovic, P. Marton, J. Hlinka, U. Bangert, S. Leake, P. Zubko, *Nat. Mater.* **2021**, 20, 495.
- [16] V. Anbusathaiah, D. Kan, F. C. Kartawidjaja, R. Mahjoub, M. A. Arredondo, S. Wicks, I. Takeuchi, J. Wang, V. Nagarajan, *Adv. Mater.* **2009**, 21, 3497.
- [17] Y. Zhang, M. G. Han, J. A. Garlow, Y. Tan, F. Xue, L. Q. Chen, P. Munroe, N. Valanoor, Y. Zhu, *Nano Lett.* **2019**, 19, 5319.
- [18] R. V. K. Mangalam, J. Karthik, A. R. Damodaran, J. C. Agar, L. W. Martin, *Adv. Mater.* **2013**, 25, 1761.
- [19] P. Kavle, A. M. Ross, J. A. Zorn, P. Behera, E. Parsonnet, X. Huang, C. Lin, L. Caretta, L. Chen, L. W. Martin, *Adv. Mater.* **2023**, 35, 2301934.
- [20] Z. Chen, Y. Jiang, Y.-T. Shao, M. E. Holtz, M. Odstrčil, M. Guizar-Sicairos, I. Hanke, S. Ganschow, D. G. Schlom, D. A. Muller, *Science* **2021**, 372, 826.
- [21] A. M. Maiden, M. J. Humphry, J. M. Rodenburg, *J. Opt. Soc. Am. A* **2012**, 29, 1606.
- [22] H. Aramberri, N. S. Fedorova, J. Iniguez, *Sci. Adv.* **2022**, 8, 1.
- [23] R. Guo, L. E. Cross, S. E. Park, B. Noheda, D. E. Cox, G. Shirane, *Phys. Rev. Lett.* **2000**, 84, 5423.
- [24] J. Kim, A. Kumar, Y. Qi, H. Takenaka, P. J. Ryan, D. Meyers, J. W. Kim, A. Fernandez, Z. Tian, A. M. Rappe, J. M. LeBeau, L. W. Martin, *Nat. Phys.* **2022**, 18, 1502.
- [25] M. Acharya, D. Lou, A. Fernandez, J. Kim, Z. Tian, L. W. Martin, *Phys. Rev. Appl.* **2023**, 20, 014017.
- [26] M. W. Tate, P. Purohit, D. Chamberlain, K. X. Nguyen, R. Hovden, C. S. Chang, P. Deb, E. Turgut, J. T. Heron, D. G. Schlom, D. C. Ralph, G. D. Fuchs, K. S. Shanks, H. T. Philipp, D. A. Muller, S. M. Gruner, *Microsc. Microanal.* **2016**, 22, 237.
- [27] E. H. R. Tsai, I. Usov, A. Diaz, A. Menzel, M. Guizar-Sicairos, *Opt. Express* **2016**, 24, 29089.
- [28] P. Thibault, M. Guizar-Sicairos, *New J. Phys.* **2012**, 14, 063004.
- [29] C. Zhang, Y.-T. Shao, Z. Baraissov, C. J. Duncan, A. Hanuka, A. L. Edelen, J. M. Maxson, D. A. Muller, *Microsc. Microanal.* **2022**, 28, 3146.
- [30] K. P. Harikrishnan, D. Yoon, Y.-T. Shao, L. Mele, C. Mitterbauer, D. Muller, *Microsc. Microanal.* **2021**, 27, 1994.
- [31] E. Padgett, M. E. Holtz, P. Cueva, Y. T. Shao, E. Langenberg, D. G. Schlom, D. A. Muller, *Ultramicroscopy* **2020**, 214, 112994.
- [32] M. Nord, P. E. Vullum, I. MacLaren, T. Tybell, R. Holmestad, *Adv. Struct. Chem. Imaging* **2017**, 3, 9.
- [33] S. J. Pennycook, D. E. Jesson, *Ultramicroscopy* **1991**, 37, 14.
- [34] J. Wu, J. Yang, L. Ma, L. Zhang, S. Liu, *Phys. Rev. B* **2023**, 107, 1.
- [35] S. Plimpton, *J. Comput. Phys.* **1995**, 117, 1.
- [36] A. M. Ross, L. Q. Chen, *Acta Mater.* **2023**, 261, 119405.
- [37] J. J. Wang, X. Q. Ma, Q. Li, J. Britson, L. Q. Chen, *Acta Mater.* **2013**, 61, 7591.
- [38] R. Uecker, B. Velickov, D. Klimm, R. Bertram, M. Bernhagen, M. Rabe, M. Albrecht, R. Fornari, D. G. Schlom, *J. Cryst. Growth* **2008**, 310, 2649.
- [39] G. Kresse, J. Furthmüller, *Comput. Mater. Sci.* **1996**, 6, 15.
- [40] G. Kresse, J. Furthmüller, *Phys. Rev. B – Condens. Matter Mater. Phys.* **1996**, 54, 11169.
- [41] D. Joubert, *Phys. Rev. B – Condens. Matter Mater. Phys.* **1999**, 59, 1758.
- [42] P. E. Blöchl, *Phys. Rev. B* **1994**, 50, 17953.
- [43] J. P. Perdew, A. Ruzsinszky, G. I. Csonka, O. A. Vydrov, G. E. Scuseria, L. A. Constantin, X. Zhou, K. Burke, *Phys. Rev. Lett.* **2008**, 100, 136406.